ECL chemiluminescence system (GE Healthcare). We quantified the protein expressions by using Scion Image software.

RGM-binding assay. We incubated splenocytes with different concentrations of human RGM-Fc for 30 min, washed and immunostained them with CD11b-specific PE-conjugated or CD4-specific APC-conjugated (BD Bioscience) antibody in combination with human Fc-specific FITC-conjugated antibodies (Sigma-Aldrich), and performed flow cytometric analysis. For analytical flow cytometry, we collected at least 10,000 events of lymphocytes on a BD Biosciences fluorescent-activated cell sorter (Calibur) and analyzed the data by using CellQuest software (BD Biosciences). We included the antibody isotype control for RGM-Fc staining and subtracted the level of background staining from the level of RGM-Fc staining.

Rap1 activity assay *in vitro* and *in vivo*. We measured Rap1 activity by using a Rap1 activation assay kit (Upstate Biotechnology). In brief, we treated $CD4^+$ T cells or splenocytes with or without 2 μg ml^{-1} of mouse recombinant RGMa (R&D Systems) for 5 min and lysed them in Mg^{2+} lysis buffer containing 25 mM *N*-2-hydroxyethylpiperazine-*N*′-2-ethanesulphonic acid (pH 7.5), 150 mM NaCl, 1% Igepal CA-630, 10 mM $MgCl_2$, 1 mM ethylenediaminetetraacetic acid, 2% glycerol, 2 mM sodium orthovanadate, 1 mM ethylsulfonyl fluoride, and protease inhibitor cocktails (Roche Diagnostics). We used cell lysates for estimating the total amount of Rap1. To precipitate active Rap1, we treated the cell lysates with the Ral-binding domain of the RalGDS–agarose conjugate for 30 min at 4 °C. We then washed the beads with the Mg^{2+} lysis buffer and resuspended them in 2× sample buffer for Western blotting using Rap1-specific antibodies (BD Bioscience) as described above.

We performed *in situ* detection of active Rap1 as described previously[22]. We fixed tissues in 4% paraformaldehyde (PFA) in 0.1 M phosphate buffer, incubated cryostat sections (10 μm) with blocking solution containing 5% bovine serum albumin (BSA) and 0.1% Triton X-100 in PBS for 1 h, and incubated them overnight at 4 °C in control glutathione S-transferase (GST) or GST-RalGDS (10 μg ml^{-1}). We washed the sections thrice, fixed them in 2% PFA in 0.1 M phosphate buffer for 10 min at room temperature, and washed them again. Then, we incubated them in GST-specific antibody (Santa Cruz Biotechnology) and CD4-specific antibody (BD Pharmingen) for 2 h at room temperature. We detected the signal by incubation with Alexa Fluor 488-conjugated antibody to mouse IgG and Alexa Fluor 546-conjugated antibody to rabbit IgG (Invitrogen) for 1 h at room temperature.

Lymphocyte-binding assay. We assessed cell adhesion as previously described[23,24]. In brief, flat-bottom Maxisorp 96-well plates (Nunc) were left uncoated (control) or precoated with 2 μg ml^{-1} recombinant mouse ICAM-1-Fc (for $CD4^+$ T cells; R&D Systems) overnight at 4 °C. We washed the plates with PBS and blocked the nonspecific binding sites with 2% BSA in RPMI-1640 medium (Invitrogen) for 1 h at 37 °C. We labeled purified $CD4^+$ T cells with 2.5 μM 2′,7′-bis-(2-carboxyethyl)-5-(and-6)-carboxyfluorescein acetoxymethyl ester (BCECF-AM; Calbiochem) for 30 min at 37 °C, followed by further washes with RPMI-1640 medium containing 0.5% BSA. We added a total of 5×10^5 cells to the precoated plates and incubated them for 1 h at 37 °C in 0.5% BSA–RPMI-1640 with or without 2 μg ml^{-1} recombinant RGMa. Where indicated, we pretreated $CD4^+$ cells with 20 μM of GGTI-298 (Calbiochem) for 1 h. We removed the nonadherent cells by washing the culture thrice with warm 0.5% BSA–RPMI-1640. We quantified adhesion by using SpectraMAX (Molecular Devices) at an excitation wavelength of 485 nm and emission wavelength of 538 nm. We quantified specific adhesion by subtracting the total number of fluorescent-positive cells in

the untreated wells. The adhesion was expressed as a ratio of specific cell attachment divided by the total input cell number.

In another experiment (**Fig. 4d**), we immunized mice with myelin oligodendrocyte glycoprotein (MOG) and complete Freund's adjuvant. At d 21 after the induction of EAE, we labeled freshly isolated $CD4^+$ T cells with BCECF-AM and incubated the cells with or without RGMa-specific antibody. We then calculated the ratio of specific cell attachment.

Immunohistochemical staining of mouse tissues. After 1, 2, and 3 weeks from EAE induction, we perfused mice transcardially with 4% PFA in PBS. We postfixed their spleen, lymph node, spinal cord, and brain tissues in the same fixatives at 4 °C overnight; soaked them in 30% sucrose and PBS; and then embedded them in optimal cutting temperature compound. We cut frozen cross-sections at 5 or 10 μm with a cryostat and mounted them on Matsunami adhesive silane-coated slides. We permeabilized the sections in PBS containing 0.1% Triton-X100, 10% goat serum, and 1% BSA for 1 h at room temperature and then incubated them with primary antibodies overnight at 4°C, followed by incubation with fluorescence-conjugated secondary antibodies for 1 h at room temperature. We used the following primary antibodies: RGMa-specific rabbit (IBL), neogenin-specific rabbit (Santa Cruz Biotech), CD11b-specific rat (Serotec), CD4-specific rat (BD Bioscience), mPDCA-1-specific rat (Miltenyi Biotec), CD11c-specific hamster (BD Bioscience), B220-specific rat (BD Bioscience), APP-specific rabbit (Invitrogen), and F4/80-specific rat (Serotec) antibodies. We used Alexa Fluor 488- or 568-conjugated goat antibody to rabbit IgG, goat antibody to rat IgG, and goat antibody to hamster IgG (Invitrogen) as the secondary antibodies. For quantification of the immunofluorescence intensities in each cell, we traced the contour of the cell manually on a counterstained image of the corresponding cell-type marker. We determined the fluorescence intensities for RGMa or neogenin within the contour

of the cell. We determined the background fluorescence of the cells by performing an identical analysis with cells labeled in the absence of the primary antibodies. We then averaged the values of the background fluorescence intensity from twenty cells and subtracted these values from the signals obtained by the immunofluorescent staining[25]. We determined the average intensities for 50–100 cells from each animal and normalized the relative intensities by using those of the controls.

To assess demyelination in the spinal cord, we performed myelin staining by using a green fluorescent lipophilic dye (FluoroMyelin, Invitrogen) according to the manufacturer's instructions; we also double-labeled the section with 4′,6-diamidino-2-phenylindole (DAPI). We identified demyelinating lesions in the ventral white matter as regions without FluoroMyelin staining.

Immunohistochemical staining of human tissues and PBMCs. We obtained tissue samples and PBMCs of individuals with MS from Chiba University, Kitasato University, and Aichi Medical University. We fixed the brain and spinal cord samples in formalin, embedded them in paraffin, and cut them in 4-μm-thick sections for immunohistochemistry. We then deparaffinized, washed, and subjected the sections to an antigen-retrieval procedure. We incubated tissue samples with human CD83-specific mouse (Serotec) or human CD209-specific (BD Pharmingen) antibodies together with human RGMa-specific antibodies (R&D System). In another experiment, we incubated the tissue samples with human CD3-specific antibody (Dako) and human neogenin-specific antibody (Santa Cruz Biotechnology). We used Alexa Fluor 488- or 568-conjugated goat anti-mouse IgG and goat anti-rat IgG (Invitrogen) as the secondary antibodies.

We sedimented the PBMCs on polyethylenimine-coated glass slides. For staining, we fixed the cells in 4% PFA in PBS and incubated them with human CD3-specific antibody and

human neogenin-specific antibody. Alexa Fluor 488-conjugated goat anti-rabbit IgG and 568-conjugated goat anti-mouse IgG (Invitrogen) were used as the secondary antibodies. We determined the fluorescence intensities for neogenin within the contour of each cell, and determined and subtracted the background fluorescence intensity. We determined the average intensities in 50–100 cells from each sample and normalized the relative intensities by using those of the controls.

EAE scoring. We assessed clinical signs of EAE on the basis of the following scale: 0, no abnormalities noted; 0.5, loss of tail tonicity; 1, loss of tail reflex; 2, loss of tail reflex, impaired righting, and paresis of one limb; 3, paresis and paralysis of one limb; 3.5, full hind limb paralysis; 4, front and hind limb paralysis; and 5, moribund or dead. We assigned intermediate scores if the neurological signs were intermediate between two scores. We obtained the mean cumulative score by averaging the total clinical scores of each mouse with EAE after immunization.

Histopathology. In the histological evaluation, we stained PFA-fixed, paraffin-embedded sections of the spinal cord with hematoxylin and eosin to assess inflammation. We examined 20–30 transverse sections from the cervical to thoracic spinal cord per mouse. We scored inflammation (inflammatory index) as follows: 0, no inflammation; 1, cellular infiltration only in the perivascular areas and meninges; 2, mild cellular infiltration in the parenchyma; 3, moderate cellular infiltration in the parenchyma; and 4, severe cellular infiltration in parenchyma[26,27].

Knockdown experiments with siRNA. We synthesized mouse RGMa siRNA (stealth siRNA,

Invitrogen) and mouse neogenin siRNA (Sigma-Genosys). The sense and antisense strands of RGMa siRNA were 5′-AAAGAGGCCGCAGUGAGUGUAGUUG-3′ and 5′-CAACUACACUCACUGCGGCCUCUUU-3′, respectively, and those of neogenin siRNA were 5′-CAAUUCCAUGGAUAGCAAU-3′ and 5′-AUUGCUAUCCAUGGAAUUG-3′, respectively. We transfected RGM siRNA, neogenin siRNA, and nontargeting double-stranded RNA (control mismatch siRNA; Invitrogen) into BMDCs and BMMØs by using Nucleofector (Amaxa, Inc.) according to the manufacturer's instructions. We estimated the transfection efficiency by using BLOCK-iT Alexa Fluor Red Fluorescent Oligo (Invitrogen) at ~50%. We collected the BMDCs and BMMØs on d 7 and washed them twice in PBS. Subsequently, we suspended 1×10^6 cells in 100 μl of nucleofection solution for mouse dendritic cells or macrophages (Amaxa, Inc.) containing 500 pmol of mouse RGMa siRNA, neogenin siRNA, or control siRNA. We transferred the samples into the certified cuvettes and placed them in the Nucleofector device. We accomplished nucleofection of the cells by using the AN-001 program (BMDCs) and Y-001 program (BMMØs). After the transfection, we cultured the cells in complete medium containing RPMI-1640 medium supplemented with glutamine, sodium pyruvate, penicillin, streptomycin, 2-ME, and 10% heat-inactivated fetal bovine serum (FBS).

GFP-labeled cell transfer and trafficking analysis. We performed cell transfer experiments by intravenous injection of 5×10^6 $CD4^+$ T cells derived from MOG-induced EAE C57BL/6-Tg (CAG-EGFP) mice into recipient wild-type mice. We immunized CAG-EGFP mice with MOG, and isolated splenocytes from them on d 7 after immunization, followed by re-stimulation with MOG for 3 d. We treated recipient mice with control or RGMa-specific antibody 3 d before and at the transfer of the restimulated $CD4^+$ T cells. Ten d after adoptive transfer, we transcardially perfused the mice with 4% paraformaldehyde in PBS. We dissected

the brain and cervical spinal cord, fixed them in the same fixatives overnight at 4 °C, and immersed them in 30% sucrose in PBS. Serial sections (20-μm thick) were cut using a cryostat and mounted on MAS-coated slides. We immunostained these sections with a rabbit GFP-specific antibody (Invitrogen) to detect EGFP-labeled cells. We counted the number of the GFP^+ T cells in sections by a standardized protocol for estimating cell density, which involved counting the number of GFP^+ T cells in the forebrain including the lateral ventricle, and the cervical spinal cord. Sections (5–10) with an individual distance of 200 μm were examined in the brain and spinal cord of the normal mice (n = 5) and RGMa-specific antibody-treated mice (n = 5).

Migration assay. We used murine brain-derived capillary endothelial cell line b-End3 (American Type Culture Collection) for this experiment. The culture medium consisted of Dulbecco's modified Eagle's medium supplemented with 2% penicillin plus streptomycin and 10% FBS. The cells were grown to confluence in the upper chamber of a 3-μm-pore 24-well transwell insert (Millipore), shown to induce and maintain blood–brain barrier characteristics *in vitro*. We evaluated barrier function in the cell monolayer by transepithelial electrical resistance measurements performed with Millicell-ERS. The resistance of blank filters as the background resistance was subtracted from the total resistance of each culture insert. At d 11 after EAE induction, we prepared $CD4^+$ T cells from MOG-EAE mice treated with control IgG or RGMa-specific antibody on d 7 and 10 after MOG immunization. We loaded a suspension of 1×10^6 $CD4^+$ T cells ml^{-1} in the upper chamber, in the presence of 10 μg ml^{-1} of RGMa-specific antibody or control antibody. We assessed the ability of $CD4^+$ T cells to cross the monolayer by counting the number of cells that transmigrated to the lower chamber after 18 h.

Adoptive transfer experiments. For the adoptive transfer of macrophages with neogenin knockdown, we injected CD11b-DTR mice intravenously with 5×10^6 live BMMØs with or without neogenin knockdown. Because CD11b is positive for certain dendritic cells, we injected mice simultaneously with 5×10^6 BMDCs. We then immunized the mice with MOG, injected subcutaneously with 0.2 ml CFA containing 500 μg of *Mycobacterium tuberculosis*. Recipient mice received 200 ng of pertussis toxin intravenously 48 h after the MOG immunization. For ablation of resident macrophages, we injected the CD11b-DTR mice intraperitoneally with 25 ng g^{-1} diphtheria toxin (Sigma) on d –1 and 3 after the MOG immunization.

Intrathecal administration of RGMa-specific antibody in EAE mice. On d 7 after the MOG-EAE induction, we fitted the mice with an osmotic minipump (100 μl solution, 0.5 μl h^{-1}, 7-d delivery; Alzet pump model 1007D) filled with control rabbit IgG (22.3 μg kg^{-1} d^{-1} over 1 week; Sigma-Aldrich) or RGMa-specific antibody (22.3 μg kg^{-1} d^{-1} over 1 week). This antibody dose has been shown to be effective in inhibiting the effect of RGMa in the CNS[10]. We placed the minipump under the skin of the animal's back and connected a Silastic tube to the minipump under the dura of the thoracic cord. We sutured the tube just caudal to the laminectomy site to anchor it in place. Afterward, we sutured the muscle and skin layers.

Animal model of spinal cord injury and behavioral analysis. We anesthetized female C57BL/6 mice with sodium pentobarbital (40 mg kg^{-1}) and performed laminectomy at the T9–T10 vertebral level. The mice then received a moderate (60 kdyn) contusion injury with an Infinite Horizons impactor. We intraperitoneally administered 400 μg of RGMa-specific or control antibody (rabbit IgG; Sigma-Aldrich) to the mice on d 0 and 3 after the injury. To assess their functional recovery after the injury, two blinded observers tested the mice by

using the open-field Basso Mouse Scale (BMS)[28] on d 1, 3, and 5, and once a week thereafter until the end of the study. We plotted the mean scores per treatment group as a function of the time post-injury. We also performed manual bladder expression twice a day until reflex bladder emptying was established. We had assessed the animals before the injury to ensure the absence of deficits in hind limb function and expose them to an open-field testing environment.

PBMC isolation and stimulation. We isolated all PBMCs freshly by using standard Ficoll-Hypaque centrifugation within 24 h of venipuncture and immediately applied them to the following assays. We pretreated PBMCs with 10 μg ml^{-1} of mouse monoclonal human RGMa-specific antibody, which we generated, or with control IgG for 30 min and then stimulated them with PMA (10 ng ml^{-1}) and ionomycin (1 μg ml^{-1}) (both from Sigma-Aldrich) in RPMI-1640 medium supplemented with glutamine, sodium pyruvate, penicillin, streptomycin, 2-ME, and 10% heat-inactivated FBS. We estimated the cell proliferation by measuring the BrdU incorporation and estimated the production of *IL-2*, *IFN-γ*, *IL-17*, *IL-4*, *IL-10*, and *TGF-β* by RT-PCR analysis.

Biodistribution of RGMa-specific antibody. We administered RGMa-specific antibody (400 μg intraperitoneally) to mice on d 0 and 2. We anesthetized the mice and removed their spleen, lymph node, spinal cord, and brain tissues on d 7 for biodistribution analysis of RGMa-specific antibody. We lysed the tissues and subjected them to Western blotting with horseradish peroxidase-conjugated rabbit IgG antibody (Cell Signaling Technology). We also administered RGMa-specific antibody by intraperitoneal injection to the mice on d 7 and 10 after the MOG immunization and assessed the biodistribution on d 11.

Intracellular staining. We analyzed intracellular cytokine expressions in freshly isolated splenocytes stimulated with CD3-specific antibody in the presence of 10 μg ml^{-1} Brefeldin A (Sigma-Aldrich) for 6 h. After staining the cells with a phycoerythrin-conjugated CD4-specific antibody (BD Biosciences), we fixed and permeabilized (Cytofix/Cytoperm and Perm/Wash buffer; BD Biosciences) and stained them with FITC-conjugated IL-4- or IL-10-specific (BD Biosciences) antibody, and then analyzed the results fluorocytometrically (FACSCalibur; BD Biosciences).

SUPPLEMENTARY REFERENCES

21. Lutz, M.B. *et al.* An advanced culture method for generating large quantities of highly pure dendritic cells from mouse bone marrow. *J. Immunol. Methods* **223**, 77–92 (1999).

22. Taniguchi, J. *et al.* Rap1 is involved in the signal transduction of myelin-associated glycoprotein. *Cell Death Differ.* **15**, 408–419 (2008).

23. Sebzda, E., Bracke, M., Tugal, T., Hogg, N. & Cantrell, D.A. Rap1A positively regulates T cells via integrin activation rather than inhibiting lymphocyte signaling. *Nat. Immunol.* **3**, 251–258 (2002).

24. Duchniewicz, M. *et al.* Rap1A-deficient T and B cells show impaired integrin-mediated cell adhesion. *Mol. Cell Biol.* **26**, 643–653 (2006).

25. Alexander, J.K. *et al.* Ric-3 promotes α7 nicotinic receptor assembly and trafficking through the ER subcompartment of dendrites. *J. Neurosci.* **30**, 10112–10126 (2010).

26. Okuda, Y., Okuda, M. & Bernard, C.C. The suppression of T cell apoptosis influences the severity of disease during the chronic phase but not the recovery from the acute phase of experimental autoimmune encephalomyelitis in mice. *J. Neuroimmunol.* **131**, 115–125 (2002).

27. Liu, J. *et al.* TNF is a potent anti-inflammatory cytokine in autoimmune-mediated demyelination. *Nat. Med.* **4**, 78–83 (1998).

28. Basso, D.M. *et al.* Basso Mouse Scale for locomotion detects differences in recovery after spinal cord injury in five common mouse strains. *J. Neurotrauma* **23**, 635–659 (2006).

The EMBO Journal (2011) 30, 1389–1401 | © 2011 European Molecular Biology Organization | All Rights Reserved 0261-4189/11
www.embojournal.org

THE EMBO JOURNAL

Myelin suppresses axon regeneration by PIR-B/SHP-mediated inhibition of Trk activity

Yuki Fujita[1,2], Shota Endo[3], Toshiyuki Takai[3] and Toshihide Yamashita[1,2,*]

[1]Department of Molecular Neuroscience, Graduate School of Medicine, Osaka University, Osaka, Japan, [2]JST, CREST, Tokyo, Japan and [3]Department of Experimental Immunology and CREST Program of JST, Institute of Development, Aging and Cancer, Tohoku University, Sendai, Japan

Paired immunoglobulin-like receptor B (PIR-B) partially mediates the regeneration-inhibiting effects of the myelin-derived protein Nogo, myelin-associated glycoprotein (MAG), and oligodendrocyte-myelin glycoprotein (OMgp). In this study, we report that inhibition of the PIR-B signaling cascades in neurons enhances axon regeneration in the central nervous system (CNS). Binding of MAG to PIR-B led to the association of PIR-B with tropomyosin receptor kinase (Trk) neurotrophin receptors. Src homology 2-containing protein tyrosine phosphatase (SHP)-1 and SHP-2, which were recruited to PIR-B upon MAG binding, functioned as Trk tyrosine phosphatases. Further, SHP-1 and SHP-2 inhibition reduced MAG-induced dephosphorylation of Trk receptors and abolished the inhibitory effect of MAG on neurite growth. Thus, PIR-B associated with Trk to downregulate basal and neurotrophin-regulated Trk activity through SHP-1/2 in neurons. Moreover, *in vivo* transfection of small interfering RNA (siRNA) for SHP-1 or SHP-2 induced axonal regeneration after optic nerve injury in mice. Our results thus identify a new molecular target to enhance regeneration of the injured CNS.

The EMBO Journal (2011) **30,** 1389–1401. doi:10.1038/emboj.2011.55; Published online 1 March 2011
Subject Categories: neuroscience
Keywords: axon regeneration; myelin; paired immunoglobulin-like receptor B (PIR-B); Src homology 2-containing protein tyrosine phosphatase (SHP); tropomyosin receptor kinase (Trk)

Introduction

Myelin-derived inhibitors of axonal regeneration have an important role in inhibiting regeneration in the adult central nervous system (CNS) (Yiu and He, 2006). Three myelin-derived proteins possess potent inhibitory activity for neurite growth *in vitro* by interacting with the Nogo receptor (NgR). However, in a previous *in vitro* study, researchers have reported that genetic deletion of NgR does not reduce neurite growth inhibition by myelin-derived proteins (Zheng *et al*, 2005). This observation suggested the existence of other hitherto unidentified binding receptors for these inhibitors. Later, paired immunoglobulin-like receptor B (PIR-B)—a major histocompatibility complex (MHC) class I receptor (Takai, 2005)—was identified as a second receptor (Atwal *et al*, 2008). PIR-B is expressed on various haematopoietic cells as well as on neurons (Syken *et al*, 2006). It binds not only to the 66-amino acid long Nogo-66, which is one of the two inhibitory domains of Nogo, but also to myelin-associated glycoprotein (MAG) and oligodendrocyte-myelin glycoprotein (OMgp). Further, the presence of PIR-B is essential for inhibition of neurite growth mediated by Nogo-66 and other myelin proteins (Atwal *et al*, 2008). It is unknown whether PIR-B inhibition promotes axonal regeneration after injury to the CNS *in vivo*. Nonetheless, the role of PIR-B in restricting plasticity during development is supported by the fact that deprivation-induced expansion of the open eye's territory is more robust and can be properly induced after the critical developmental period in mice expressing PIR-B lacking the transmembrane domain (PIR-B-TM mice) (Syken *et al*, 2006). Therefore, we considered that elucidating the molecular mechanism underlying PIR-B signaling in neurons should increase our knowledge on the inability of injured axons to regenerate as well as on the plasticity of the developing CNS.

PIR-B contains immunoreceptor tyrosine-based inhibitory motifs. Phosphorylation of these sites upon ligand binding leads to Src homology 2-containing protein tyrosine phosphatase (SHP)-1 and SHP-2 recruitment to PIR-B, which then modulates immune signal transduction pathways. PIR-B isolated from the brain is also phosphorylated and associated with SHP-1 and SHP-2 (Syken *et al*, 2006). Thus, it would be of interest to elucidate the signaling mechanism of PIR-B in neurons by determining whether SHP phosphatase recruitment occurs upon ligand stimulation and to clarify whether SHP mediates PIR-B signaling in neurons. Thus, we aimed to identify the molecular targets of SHP-1 and SHP-2. SHP-1 has been shown to interact with and dephosphorylate several growth factor receptors, including insulin-like growth factor-1 (IGF-1), platelet-derived growth factor (PDGF), and epidermal growth factor (EGF) receptors (Tonks and Neel, 2001). Interestingly, a previous study reported that SHP-1 dephosphorylates the tropomyosin receptor kinase A (TrkA) receptor, a nerve growth factor (NGF) receptor, in PC12 cells and sympathetic neurons. Further, an enhanced association of SHP-2 with the TrkB receptor—a brain-derived neurotrophic factor (BDNF) receptor—inhibits BDNF-induced TrkB autophosphorylation and activation in cerebellar neurons (Rusanescu *et al*, 2005). These findings prompted us to hypothesize that Trk receptors are PIR-B targets in neurons (Marsh *et al*, 2003).

*Corresponding author. Department of Molecular Neuroscience, Graduate School of Medicine, Osaka University, 2-2 Yamadaoka, Suita, Osaka 565-0871, Japan. Tel.: +81 66 879 3661; Fax: +81 66 879 3669; E-mail: yamashita@molneu.med.osaka-u.ac.jp

Received: 19 October 2010; accepted: 4 February 2011; published online: 1 March 2011

In the present study, we demonstrated that PIR-B binds to and inactivates Trk neurotrophin receptors, which are known to promote neurite growth in neurons. Upon MAG activation, PIR-B recruited SHP-1 and SHP-2, which in turn dephosphorylated the Trk receptors. We suggest that reduced Trk receptor activity results in MAG-induced neurite growth inhibition. Further, the inhibition of SHP promoted axonal regeneration of the injured optic nerve *in vivo*.

Results

Trk receptors are PIR-B targets

We first examined whether PIR-B interacted with Trk receptors. COS-7 cells were transfected with haemagglutinin (HA)-tagged full-length TrkB (HA–TrkB FL) and/or full-length PIR-B constructs. The cell extracts were immunoprecipitated with anti-PIR-B or anti-HA antibodies (Figure 1A and B). Of

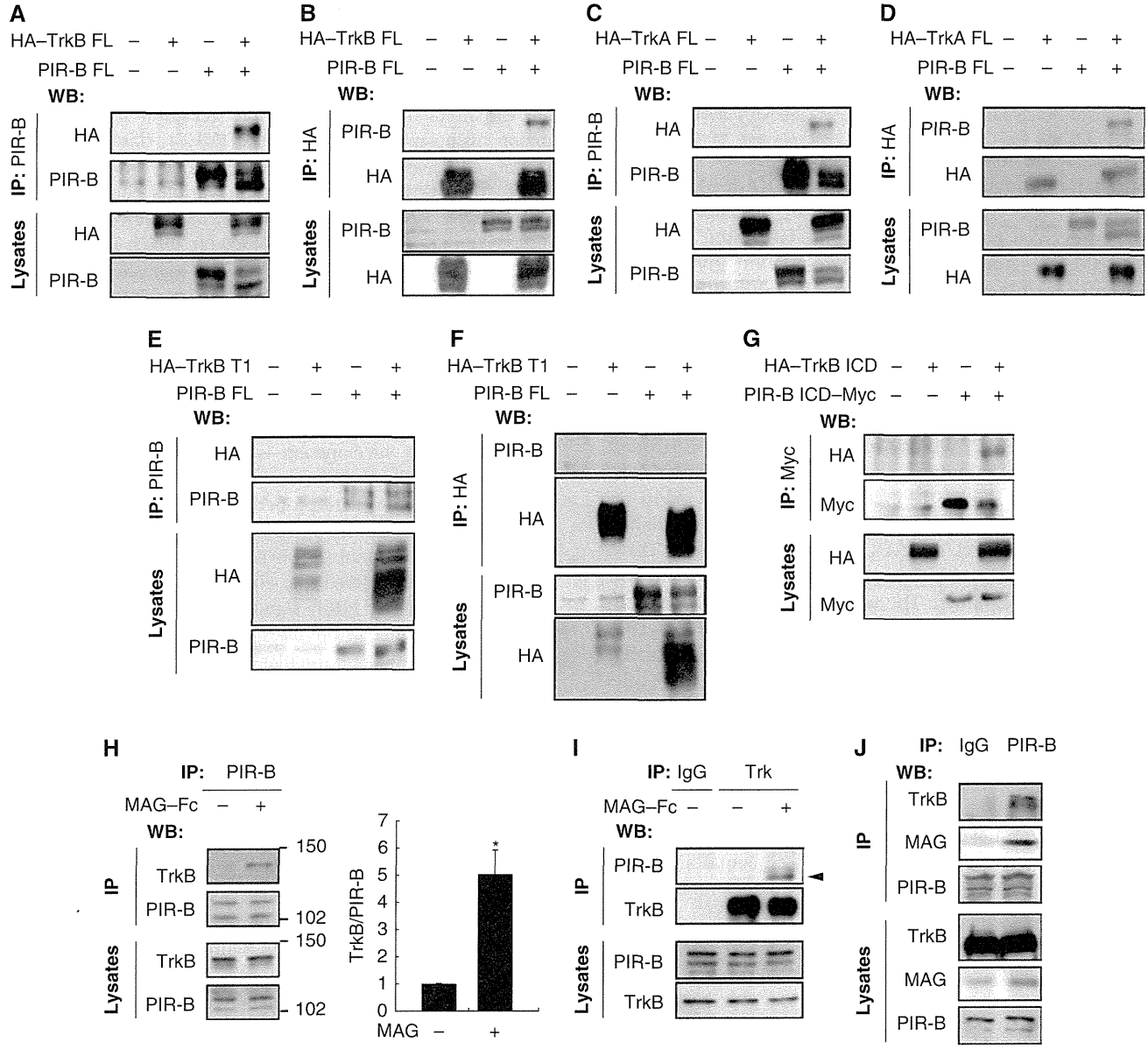

Figure 1 Ligand-dependent association of PIR-B with TrkB. (**A**, **B**) Co-immunoprecipitation of full-length PIR-B (PIR-B FL) with HA-tagged full-length TrkB (HA–TrkB FL). COS-7 cells were transiently transfected with the indicated plasmids. Cell lysates were immunoprecipitated with anti-PIR-B (**A**) or anti-HA (**B**) antibodies. The immunoprecipitates (IP) and cell lysates (lysates) were analysed by immunoblotting with anti-HA and anti-PIR-B antibodies. (**C**, **D**) Co-immunoprecipitation of PIR-B FL with HA-tagged full-length TrkA (HA–TrkA FL). COS-7 cells were transiently transfected with the indicated plasmids. Cell lysates were immunoprecipitated with anti-PIR-B (**C**) or anti-HA (**D**) antibodies. Western blotting was performed using the indicated antibodies. (**E**, **F**) PIR-B and HA-tagged TrkB T1 did not interact in the transfected COS-7 cells. Co-immunoprecipitation was carried out as shown in (**A**, **B**). (**G**) Co-immunoprecipitation of Myc-tagged PIR-B ICD (PIR-B ICD–Myc) with HA-tagged TrkB ICD (HA–TrkB ICD) using anti-Myc antibodies. (**H**, **I**) Association of endogenous PIR-B with TrkB in CGNs. CGNs were left untreated or were treated with MAG–Fc (25 μg/ml) for 15 min. Lysates prepared from the CGNs were immunoprecipitated with anti-PIR-B (**H**) or anti-pan Trk (**I**) antibodies, followed by immunoblotting with anti-TrkB and anti-PIR-B antibodies, respectively. The association between PIR-B and TrkB was observed in MAG-treated cells. IgG, control IgG. The arrowhead indicates the band corresponding to PIR-B. The TrkB signal intensity was quantified by densitometry and normalized to the signal intensity of precipitated PIR-B (**H**). $^*P<0.05$ by Welch's *t*-test. (**J**) Interaction of PIR-B with TrkB and MAG in the mouse brain. Lysates prepared from whole mouse brain were immunoprecipitated with anti-PIR-B antibodies, followed by western blotting for TrkB and MAG.

these, HA–TrkB was detected only in the HA–TrkB–PIR-B co-transfected cells precipitated with anti-PIR-B antibodies (Figure 1A). These results were consistent with those for HA–TrkB immunoprecipitation with anti-HA antibodies (Figure 1B). These findings demonstrated that ectopically expressed PIR-B interacted with TrkB in COS-7 cells. Assessment of the association of full-length TrkA and PIR-B yielded identical results (Figure 1C and D). We then investigated the molecular determinants of the PIR-B–TrkB interaction. COS-7 cells were transfected with a HA-tagged deletion construct of TrkB (HA–TrkB T1) lacking most of the intracellular domains and/or full-length PIR-B constructs (Figure 1E and F). Immunoprecipitation of the transfected cells with anti-PIR-B (Figure 1E) or anti-HA (Figure 1F) antibodies revealed no association between HA–TrkB T1 and PIR-B. Next, COS-7 cells were transfected with HA-tagged TrkB intracellular domain (HA–TrkB ICD) or PIR-B ICD. We found an interaction between HA–TrkB ICD and PIR-B ICD (Figure 1G), indicating that PIR-B associated with TrkB intracellularly, rather than extracellularly, in the transfected cells. Cell lysates expressing TrkB and PIR-B were prepared from mouse cerebellar granule neurons (CGNs) obtained on postnatal day (P) 7. A previous study has demonstrated that PIR-B is required for neurite growth inhibition in CGNs (Atwal *et al*, 2008). The cells were immunoprecipitated with anti-PIR-B antibodies and immunoblotted using anti-TrkB antibodies. TrkB was detected in the immunoprecipitates obtained using an anti-TrkB antibody after the cells were stimulated with 25 μg/ml MAG for 15 min (Figure 1H). Immunoprecipitation with an anti-TrkB or control antibody followed by immunoblotting with anti-PIR-B antibodies also yielded similar results (Figure 1I). Thus, interaction of PIR-B with TrkB in CGNs is ligand dependent. We further assessed the interaction between these proteins using lysates prepared from P7 brains. As expected, PIR-B was co-immunoprecipitated with TrkB and MAG (Figure 1J).

Association of SHP with PIR-B and TrkB

PIR-B is phosphorylated upon ligand binding and triggers the recruitment of SHP-1 and SHP-2 to PIR-B in immune cells (Takai, 2005). We evaluated the involvement of SHP in MAG signaling. CGNs were used to identify the possible association between PIR-B and SHP-2. Both SHP-2 (Figure 2A) and SHP-1 (Figure 4C) were expressed in the CGNs. The cell lysates were immunoprecipitated with an anti-PIR-B antibody or control IgG, and western blotting was performed to detect SHP-2. The association between SHP-2 and PIR-B was enhanced by MAG–Fc treatment (Figure 2A). SHP-2 immunoprecipitation yielded consistent results (Figure 2B), indicating the ligand-dependent enhancement of the PIR-B–SHP-2 interaction in CGNs. We then investigated whether TrkB associated with SHP-1 or SHP-2. COS-7 cells were transfected with HA–TrkB and PIR-B and left untreated or treated with MAG–Fc for 15 min, followed by immunoprecipitation with anti-TrkB or control IgG. SHP-2 was co-immunoprecipitated with TrkB; this association was enhanced by MAG–Fc treatment (Figure 2C). Identical results were obtained in CGNs (Figure 2D). In addition, we assessed the ligand-dependent recruitment of SHPs to PIR-B and TrkB in CGNs. Both SHP-2 and TrkB were co-immunoprecipitated with PIR-B after MAG–Fc treatment (Figure 2E). These results demonstrate that SHP-2 was recruited to PIR-B and TrkB upon MAG stimulation.

MAG stimulation induces dephosphorylation of Trk receptors by an SHP-1- and SHP-2-dependent mechanism

To explore the physiological role of the PIR-B–TrkB–SHP complex, we performed loss-of-function experiments using small interfering RNA (siRNA). We first examined if transfection with these siRNAs specifically reduced the corresponding target mRNAs. siRNA nucleofection of CGNs yielded almost 100% transfection efficiency (data not shown). Efficient downregulation of *shp1* mRNA was found specifically in SHP-1 siRNA-transfected but not SHP-2 siRNA-transfected cells (Figure 3A; 87% inhibition by SHP-1 siRNA #1 and 72% inhibition by SHP-1 siRNA #2). Similarly, SHP-2 siRNA but not SHP-1 siRNA reduced *shp2* transcript levels (Figure 3B; 84% inhibition by SHP-2 siRNA #1 and 69% inhibition by SHP-2 siRNA #2). Consistent results were obtained when we assessed the protein expression levels in these siRNA-transfected cells (Figure 3C), indicating that we successfully achieved siRNA-mediated knockdown of SHP-1 and SHP-2.

We determined that PIR-B, Trk receptors, and SHP-2 interacted in response to MAG stimulation. We then tested whether SHPs regulated Trk receptor activity. The Trk receptors were immunoprecipitated with anti-pan Trk antibodies, followed by western blotting for phosphotyrosine to detect their phosphorylation status. The CGNs, which express PIR-B and TrkB endogenously, were treated with MAG–Fc for 30 min, followed by immunoprecipitation with anti-pan Trk antibodies. We did not detect phosphotyrosine signals in the CGNs (Figure 4A, left lane). However, this result did not imply that Trk receptors were completely inactive under baseline conditions in the absence of neurotrophins; rather, it suggested that the activity was below the detection threshold determined by the sensitivity of the antibodies used (Figure 5B and C). To raise the detection threshold, we added 100 ng/ml BDNF to the culture. In this condition, Trk receptors were tyrosine dephosphorylated upon treatment of CGNs with MAG–Fc (Figure 4A). We used the SHP inhibitor 8-hydroxy-7-(6-sulphonaphthalen-2-yl)diazenyl-quinoline-5-sulphonic acid (NSC-87877) to assess whether MAG–Fc-induced dephosphorylation of Trk receptors was dependent on SHP. Pretreatment of the CGNs with NSC-87877 for 3 h significantly reduced MAG–Fc-induced dephosphorylation (Figure 4B). We then knocked down SHP-1 or SHP-2 using siRNA. Knockdown of SHP-1 or SHP-2 with the corresponding siRNAs inhibited MAG–Fc-induced dephosphorylation of the Trk receptors (Figure 4C and D). Knockdown of either SHP-1 or SHP-2 was sufficient for complete suppression of the effect of MAG on the phosphorylation state of Trk receptors; therefore, both SHP-1 and SHP-2 or a certain amount of the total activity of both phosphatases may be required for MAG–Fc-induced Trk dephosphorylation.

We further tested whether SHPs regulate phosphorylation of Trk receptors in dissociated retinal neurons. TrkB was immunoprecipitated with anti-TrkB antibodies and the phosphorylation levels of TrkB were determined. Knockdown of either SHP-1 (Figure 4E) or SHP-2 (Figure 4F) abolished MAG-induced TrkB dephosphorylation in retinal cells.

Notably, knockdown of either SHP-1 (Figure 4E) or SHP-2 (Figure 4F) *per se* enhanced TrkB phosphorylation.

We used PIR-B$^{-/-}$ mice to determine the contribution of PIR-B to the inhibitory effect of MAG–Fc. PIR-B$^{-/-}$ mice lacking the sequences encoding the sixth ectodomain and juxtamembrane domains were generated by standard gene targeting methods (Ujike *et al*, 2002). MAG–Fc-induced dephosphorylation was lower in cells isolated from PIR-B$^{-/-}$

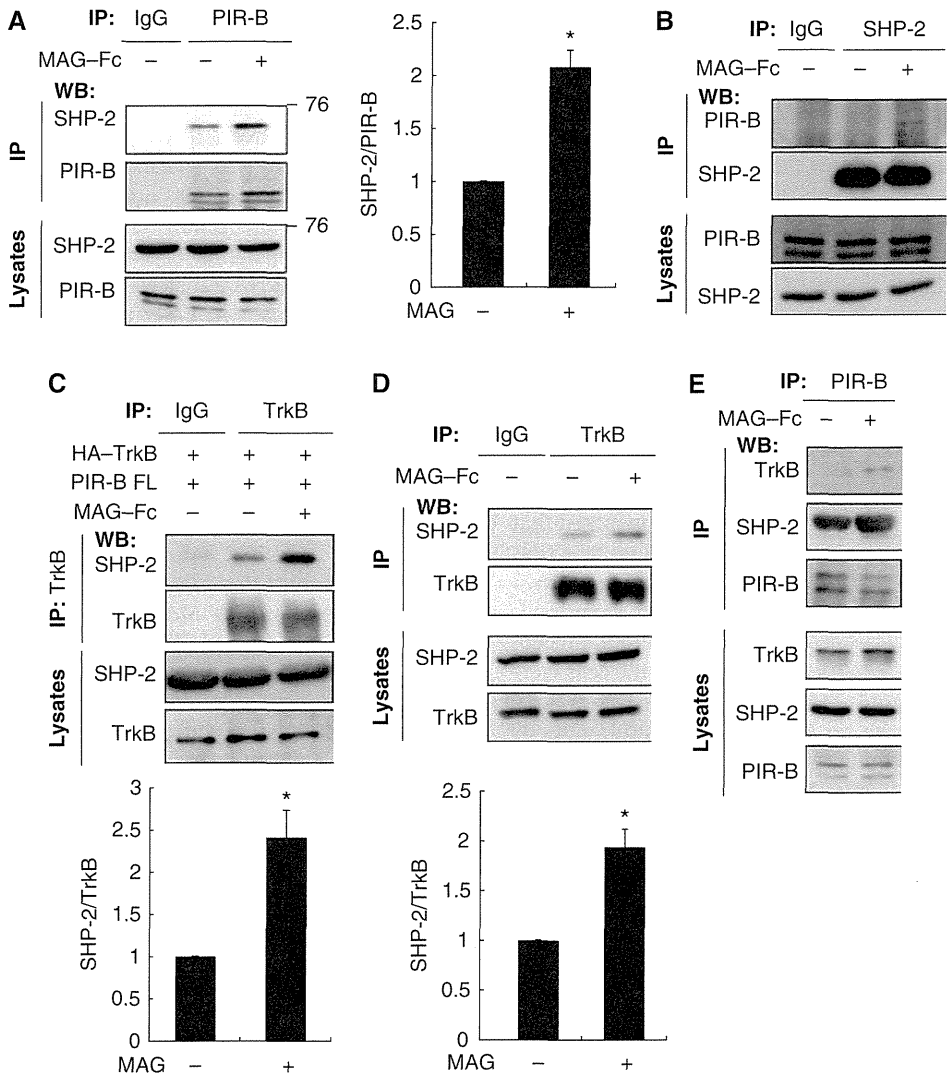

Figure 2 Co-immunoprecipitation of PIR-B with SHP-2. (**A**, **B**) Association of endogenous PIR-B with SHP-2 in CGNs. CGNs were left untreated or treated with MAG–Fc (25 μg/ml) for 15 min. The lysates were immunoprecipitated with anti-PIR-B (**A**) or anti-SHP-2 (**B**) antibodies, followed by western blotting analysis with anti-SHP-2 and anti-PIR-B antibodies, respectively. The interaction of PIR-B and SHP-2 was enhanced by treatment with MAG–Fc. The relative levels of SHP-2 were normalized to the signal intensity of the precipitated PIR-B (graph). $*P<0.05$ by Welch's *t*-test. (**C**) COS-7 cells were transfected with HA-tagged TrkB (HA–TrkB) and PIR-B, and left untreated or treated with MAG–Fc (25 μg/ml) for 15 min. The lysates were immunoprecipitated with an anti-TrkB antibody or control IgG. Association of HA–TrkB with SHP-2 was enhanced by treatment with MAG–Fc. The relative levels of SHP-2 after immunoprecipitation with TrkB are shown (graph). (**D**) CGNs were left untreated or treated with MAG–Fc (25 μg/ml) for 15 min. The lysates were immunoprecipitated with an anti-TrkB antibody or control IgG. Association of TrkB with SHP-2 was enhanced by treatment with MAG–Fc. The relative levels of SHP-2 after immunoprecipitation with TrkB are shown (graph). $*P<0.05$ by Welch's *t*-test. (**E**) PIR-B associated with TrkB and SHP-2 upon stimulation of CGNs with MAG. CGNs treated with MAG–Fc for 15 min were lysed and immunoprecipitated with an anti-PIR-B antibody, and the precipitated proteins were detected using western blotting with anti-PIR-B, anti-TrkB, and anti-SHP-2 antibodies.

Figure 3 siRNA-mediated knockdown of SHP mRNA and protein levels in CGNs. (**A**, **B**) SHP-1 and SHP-2 siRNA specifically reduced target mRNA expression. CGNs were transfected with the indicated siRNAs. Total RNA isolated at 72 h after transfection was analysed by real-time PCR. Transfection with SHP-1 siRNA reduced *shp1* transcript levels by 87% (SHP-1 siRNA #1) or 72% (SHP-1 siRNA #2) but did not affect *shp2* expression levels (**A**). Transfection with SHP-2 siRNA reduced *shp2* transcript levels by 84% (SHP-2 siRNA #1) or 69% (SHP-2 siRNA #2) but did not affect *shp1* expression levels (**B**). (**C**) SHP-1 and SHP-2 siRNA specifically reduced target protein expression. CGNs were transfected with the indicated siRNAs. Cell lysates were prepared 72 h after transfection and subjected to western blotting. (**D**, **E**) Transfection of SHP-1 (**D**) or SHP-2 (**E**) siRNA suppressed MAG-induced neurite outgrowth inhibition. The effect of MAG was rescued by co-transfection of the construct encoding SHP-1 (**D**) or SHP-2 (**E**). CGNs were transfected with the indicated siRNAs and/or expression vector. The transfected CGNs were cultured for 24 h in the presence or absence of MAG–Fc. The mean lengths of the longest neurite per neuron are shown in the graph. Representative western blots showing detection of SHP-1 (**D**) and SHP-2 (**E**) are presented (left panels). (**A**–**E**) $**P<0.01$, $*P<0.05$.

mice than in cells isolated from wild-type (WT) mice (Figure 4G), indicating that PIR-B is required for MAG–Fc-induced dephosphorylation of the Trk receptors.

We next investigated the contribution of the p75 receptor to MAG-induced TrkB dephosphorylation; p75 interacts with NgR to mediate MAG and Nogo-66 signal transduction

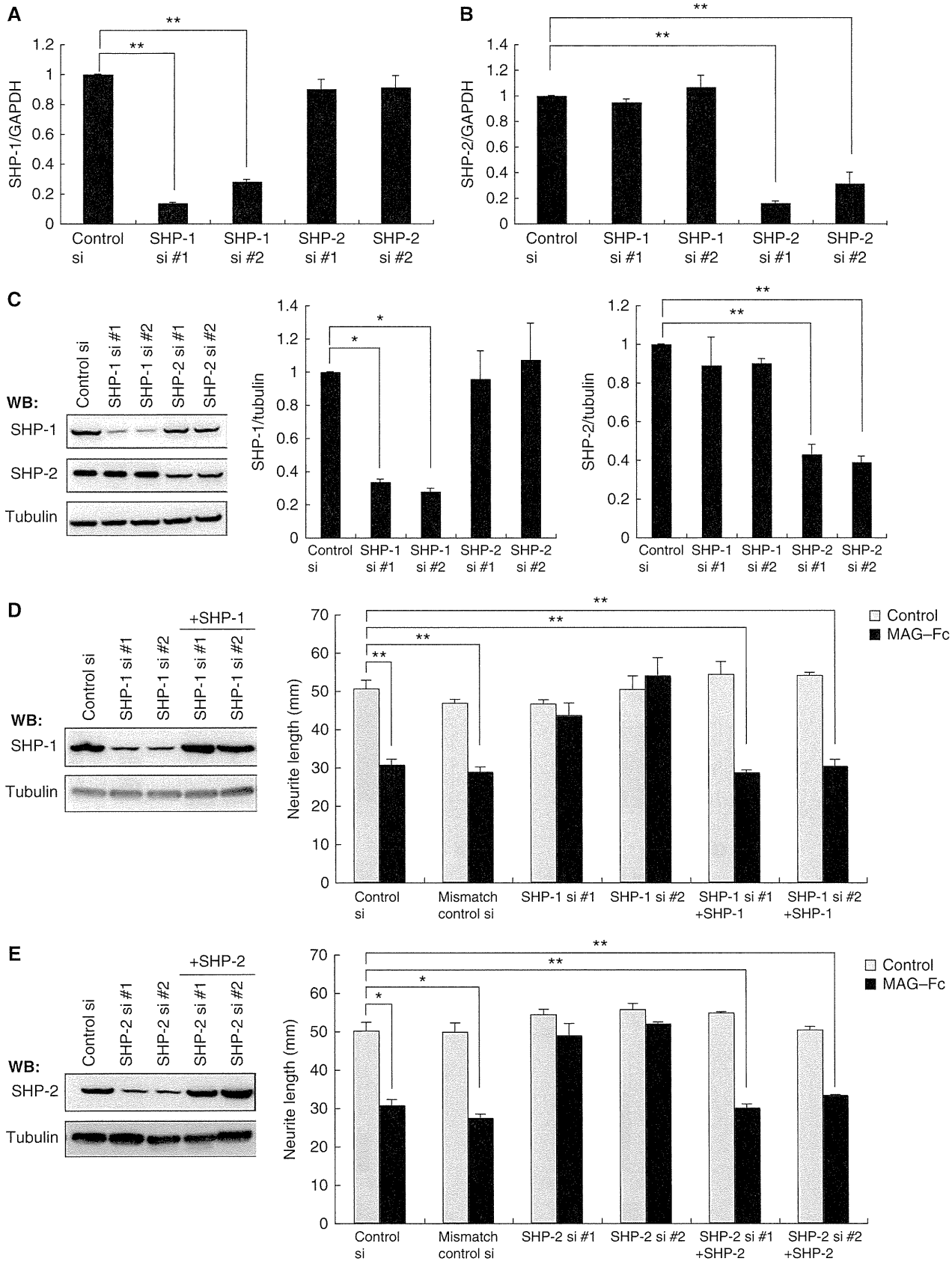

(Wang *et al*, 2002; Yamashita *et al*, 2002). In addition, p75 is a co-receptor of Trk receptors. To explore whether p75 is also required for PIR-B/TrkB signal transduction, we used CGNs isolated from mice carrying a mutation in the *p75* gene (Lee *et al*, 1992). Trk receptors of WT CGNs were tyrosine dephosphorylated upon MAG–Fc treatment. In contrast, no change was observed in CGNs isolated from mice bearing the *p75* mutation (Figure 4H). Thus, p75 is required for MAG-induced tyrosine dephosphorylation of Trk receptors.

SHP-1 and SHP-2 are required for the inhibitory effect of MAG on neurite growth in CGNs

To assess the involvement of SHP in MAG-mediated neurite growth inhibition, we compared the neurite length

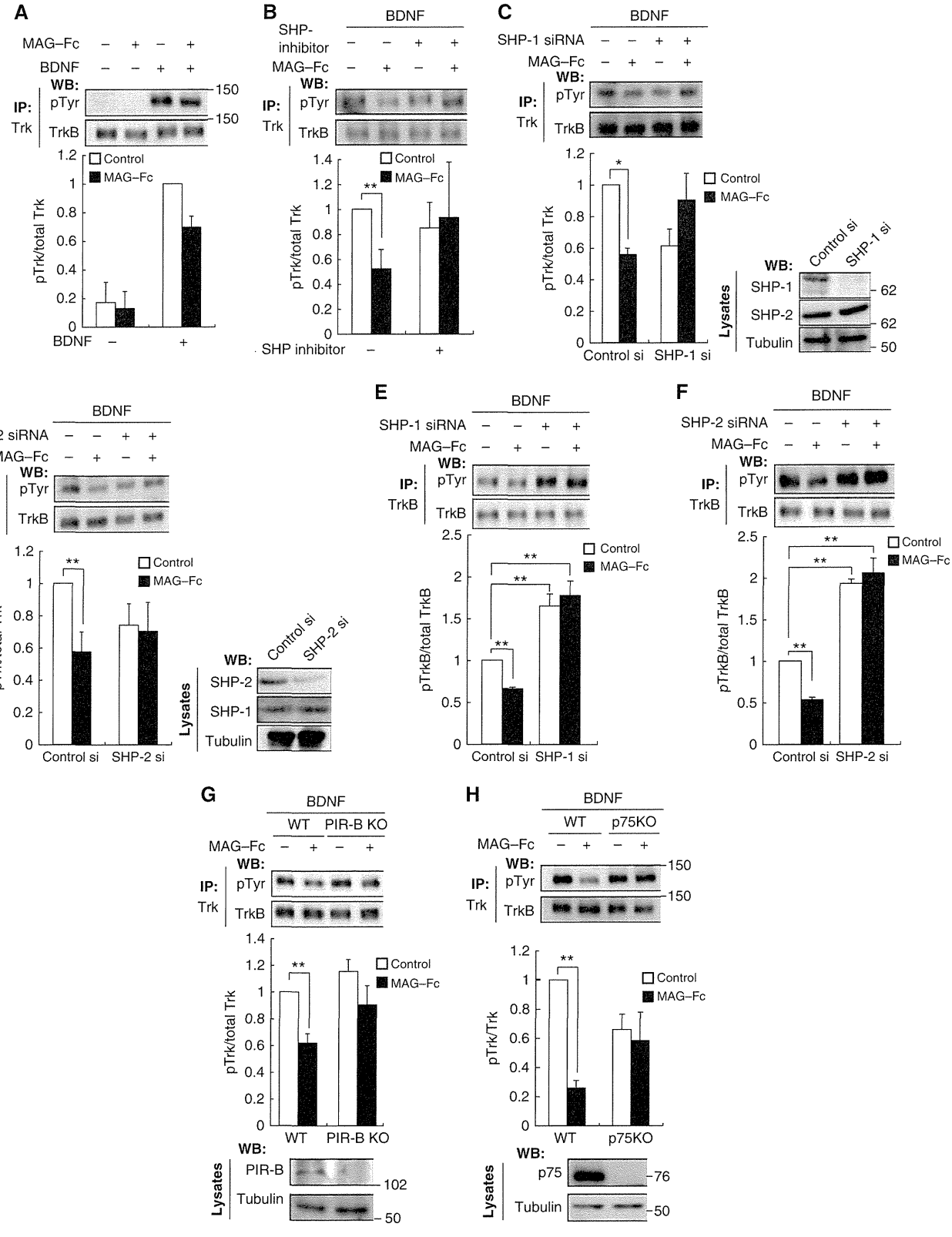

of MAG-treated and control neurons for 24 h. Neurite outgrowth in WT CGNs was significantly inhibited by MAG–Fc (Figure 5A). Using PIR-B$^{-/-}$ mice, we found that PIR-B was necessary for this effect (data not shown). This is in agreement with a previous study (Atwal *et al*, 2008). Although knockdown of SHP-1 or SHP-2 did not promote neurite growth, it reduced the inhibitory effect of MAG–Fc (Figure 3D and E). We performed rescue experiments using the same neurite growth assay in CGNs. Transfection of SHP-1 or SHP-2 cDNA in a form refractory to siRNA restored

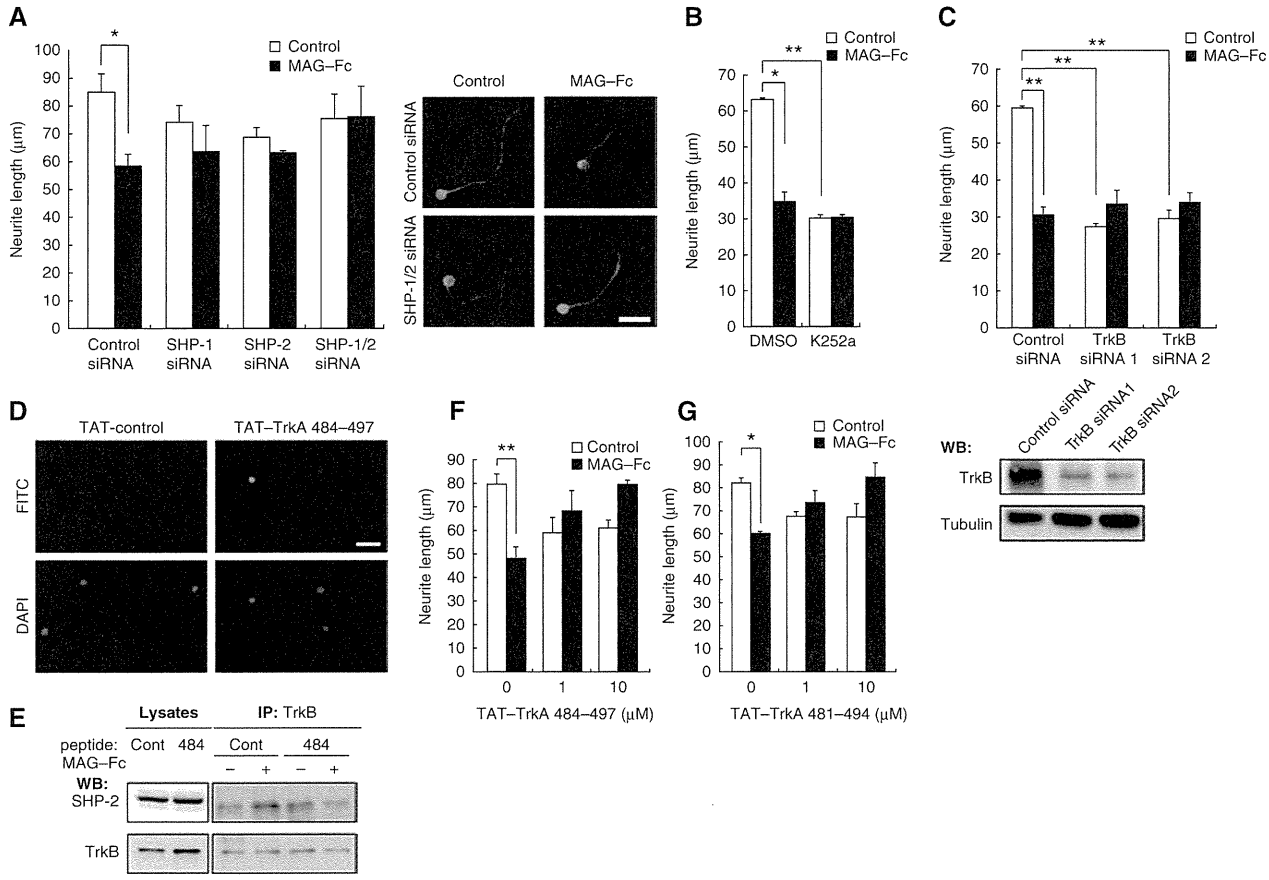

Figure 5 SHP and Trk receptors are required for the inhibitory effect of MAG. (**A**) siRNA-mediated knockdown of endogenous SHP-1 and SHP-2 suppressed the inhibitory effect of MAG–Fc on neurite growth. The transfected CGNs were cultured on poly-L-lysine-coated chamber slides for 24 h in the presence or absence of MAG–Fc. The mean lengths of the longest neurite per neuron are represented in the graph. The representative images of transfected CGNs are shown. Scale bar: 10 μm. (**B**) CGNs were cultured for 24 h with (filled bars) or without (open bars) MAG–Fc. The cells were treated with K252a 15 min before the end of the incubation period with MAG–Fc. (**C**) siRNA-mediated knockdown of endogenous TrkB attenuated the effects of MAG–Fc on neurite growth. The neurons transfected with control siRNA, TrkB siRNA #1, or TrkB siRNA #2 were cultured for 24 h in the presence or absence of MAG–Fc. Western blot analysis for TrkB in the transfected cells (lower panels). Tubulin: Tuj1. (**D**) CGNs were treated with fluorescein isothiocyanate (FITC)-conjugated TAT–TrkA 484–497 for 30 min, and the presence of the peptide in the cells was assessed. (**E**) TAT–TrkA 484–497 blocked association of TrkB with SHP-2. CGNs were pretreated with 10 μM TAT–TrkA 484–497 for 15 min and then incubated with MAG–Fc for 15 min. Co-immunoprecipitation was performed. (**F, G**) The TAT-fused peptides blocked the neurite growth inhibition induced by MAG–Fc. CGNs were pretreated with 1 or 10 μM TAT–TrkA 484–497 (**F**) or TAT–TrkA 481–494 (**G**) for 15 min, followed by incubation with MAG–Fc for 24 h. (**A–G**) $*P<0.05$, $**P<0.01$. A full-colour version of this figure is available at *The EMBO Journal* Online.

Figure 4 Inhibition of endogenous SHP reduces MAG-induced dephosphorylation of TrkB. (**A**) Stimulation with MAG reduced the tyrosine phosphorylation levels of Trk receptors. CGNs were left untreated or treated with 25 μg/ml MAG–Fc for 30 min in the presence or absence of 100 ng/ml BDNF during the final 5 min. Cell lysates were immunoprecipitated with anti-pan Trk antibodies. The immunoprecipitates (IP) were analysed by immunoblotting with anti-phospho Tyr and anti-Trk antibodies. The phosphorylation level of Trk receptors was determined by western blotting (WB: pTyr). (**B**) SHP inhibition suppressed MAG–Fc-induced dephosphorylation of Trk receptors in CGNs. CGNs were pretreated with NSC-87877 for 3 h and left untreated or stimulated with MAG–Fc as in (**A**). (**C, D**) Knockdown of SHP attenuated MAG–Fc-induced dephosphorylation of Trk receptors in CGNs. CGNs were transfected with SHP-1 (**C**), SHP-2 (**D**), or control siRNAs; 72 h after transfection, CGNs were left untreated or treated with MAG–Fc for 30 min. The right panels show that the expressions of SHP-1 (**C**) and SHP-2 (**D**) were decreased by transfection of the corresponding siRNAs. (**E, F**) Knockdown of SHP suppressed MAG–Fc-induced dephosphorylation of TrkB in retinal cells. Retinal cells were transfected with SHP-1 (**E**), SHP-2 (**F**), or control siRNAs. Knockdown of SHP-1 or SHP-2 *per se* significantly increased TrkB phosphorylation and attenuated the effects of MAG–Fc. (**G**) PIR-B is required for the MAG-induced dephosphorylation of TrkB. CGNs from WT and PIR-B KO mice were stimulated with MAG–Fc (25 μg/ml) for 30 min. (**H**) p75 is required for MAG-induced dephosphorylation of TrkB. CGNs from WT and p75-deficient mice were stimulated with MAG–Fc and BDNF. Lysates were precipitated with anti-Trk antibodies before detection with anti-phospho Tyr antibodies. (**A–H**) The graphs present the data from three independent experiments. $*P<0.05$, $**P<0.01$.

the effect of MAG on the CGNs (Figure 3D and E). Double knockdown of SHP-1 and SHP-2 completely suppressed the effect (Figure 5A). Thus, we consider that both SHP-1 and SHP-2 are necessary for MAG–Fc-induced neurite growth inhibition. Because SHP-1 and SHP-2 inhibit Trk activity, these results suggest that the basal activity of Trk receptors contributes to CGN neurite growth. MAG may inhibit neurite growth by lowering this basal activity, because no neurotrophins were added to the culture medium. To examine this hypothesis, K252a, a pan Trk inhibitor, was added to the culture medium 15 min before adding MAG, and the effect of MAG–Fc was assessed (Figure 5B). K252a mimicked the effect of MAG–Fc and significantly inhibited neurite growth. MAG–Fc did not further reduce neurite growth in K252a-treated CGNs. To rule out possible non-specific effects of this inhibitor, TrkB was knocked down by siRNA (Figure 5C, lower panels). Knockdown of TrkB significantly blocked neurite growth inhibition in CGNs and prevented MAG–Fc-induced activities (Figure 5C). These results confirmed that MAG reduces the basal activity of TrkB and inhibits neurite growth in CGNs. Finally, we determined whether the association of SHP-1/2 with TrkB is necessary for the inhibitory effect of MAG–Fc. A previous study has reported that SHP-1 interacts with TrkA at Y490 and dephosphorylates it at Y674/675 (Marsh *et al*, 2003). Based on this knowledge, we generated two TrkA peptides containing a 14-amino acid sequence comprising Y490. We then examined whether these peptides inhibit PIR-B signaling by blocking the SHP-1/2–Trk receptor interaction. To allow entrance into the cell in order to directly act on SHP-1/2 *in vivo*, the peptides were fused with the amino-terminal protein transduction domain (11 amino acids) from the human immunodeficiency virus (HIV) protein transactivator protein TAT (Schwarze *et al*, 1999) (TAT–TrkA 484–497 and TAT–TrkA 481–494). As expected, both peptides entered the CGNs efficiently within 30 min of addition (Figure 5D; only data from TAT–TrkA 484–497 are shown), and blocked the association of TrkB with SHP-2 (Figure 5E; only data from TAT–TrkA 484–497 are shown) and SHP-1 (data not shown). The addition of 1 μM TAT–TrkA 484–497 (Figure 5F) or 1 μM TAT–TrkA 481–494 (Figure 5G) to the CGN culture reduced the inhibitory effect of MAG–Fc on neurite growth. These results suggested that binding of SHP-1/2 to TrkB is critical for MAG signal transduction.

Knockdown of SHP promotes optic nerve regeneration

We assessed whether PIR-B signaling inhibition enhances axonal regeneration in the CNS. For this purpose, we employed the optic nerve crush injury model in mice. *In vivo* siRNA transfection was conducted to inhibit SHP-1 or SHP-2 in retinal cells, which expressed both SHP-1 and SHP-2 (Figure 6A). Efficient transfection of Alexa488-labeled siRNA in the retina was achieved (Figure 6B). These animals were subjected to optic nerve injury. The lysates were prepared from eye cups at 5, 11, and 14 days after injection of siRNA (Figure 6C), and the expression of each SHP isoform was examined by western blotting. The results demonstrated that the silencing effect persisted for at least 5–14 days. After *in vivo* transfection of SHP-1 (Figure 6D) or SHP-2 (Figure 6E) siRNA, the dissociated retinal cells were obtained and stimulated with MAG–Fc. Knockdown of SHP-1 (Figure 6D) or SHP-2 (Figure 6E) resulted in reduced MAG–Fc-induced dephosphorylation of TrkB. Knockdown of either isoform by itself enhanced the TrkB phosphorylation. These *in vivo* results were consistent with our above-mentioned *in vitro* findings. MAG–Fc-induced dephosphorylation of TrkB was reduced also in retinal cells from PIR-B$^{-/-}$ mice, whereas the basal level of TrkB phosphorylation was not enhanced in these cells (Figure 6F).

To assess axonal regeneration, the axons of the injured optic nerve were traced by injecting Alexa555-conjugated cholera toxin β subunit (CTB) into the vitreous humour (Figure 7A and C). The results revealed that *in vivo* optic nerve regeneration was significantly promoted by transfection of either SHP-1 siRNA or SHP-2 siRNA as compared with control siRNA, albeit the small number of regenerating axons in the optic nerve (Figure 7B and D). Thus, silencing of SHP-1 and SHP-2 contributed to the regeneration of injured axons in the optic nerve. Next, we used PIR-B$^{-/-}$ mice to determine the role of PIR-B in axon regeneration. In PIR-B$^{-/-}$ mice, the number of regenerating axons was comparable to that seen in WT mice (Figure 7E). Because downregulation of SHP-1 or SHP-2 *per se* enhanced TrkB phosphorylation (Figure 6D and E), we reasoned that activation of TrkB as well as inhibition of PIR-B may be necessary for axonal regeneration. Indeed, the basal level of TrkB phosphorylation was not enhanced in retinal cells from PIR-B$^{-/-}$ mice (Figure 6F). To test this hypothesis, we injected BDNF into the eyes of PIR-B$^{-/-}$ mice. Interestingly, BDNF injection increased axonal regeneration in PIR-B$^{-/-}$ mice but not in WT mice (Figure 7E and F). These results suggested that inhibition of PIR-B and activation of Trk receptors are necessary for axonal regeneration.

Discussion

We proposed the following molecular model for PIR-B signal transduction: first, PIR-B associates with Trk receptors, inactivating them (Figure 8); second, binding of MAG to PIR-B leads to the association of PIR-B with Trk receptors; third, SHP-1 and SHP-2, which are recruited to PIR-B upon MAG

Figure 6 *In vivo* knockdown of SHP-1 or SHP-2 in mouse retinas. (**A**) Immunohistochemical staining of SHP-1 and SHP-2 in mouse retinas. The nuclei were stained by DAPI. Scale bar: 50 μm. GCL, ganglion cell layer; INL, inner nuclear layer; ONL, outer nuclear layer. (**B**) Distribution of Alexa488-labeled siRNA in the retina after intravitreous injection. Alexa488-labeled siRNA was localized to the ganglion cells. (**C**) Western blots showing downregulation of each SHP isoform after siRNA injection. Optic nerve extracts were prepared from mice injected with control, SHP-1 #1/#2, or SHP-2 #1/#2 siRNA. At 5, 11, and 14 days after siRNA injection, lysates were prepared from the eye with the nerve segment. Representative blots from the sample prepared at 11 days after siRNA injection are shown. The signal intensity was quantified by densitometry and normalized to tubulin levels. The relative SHP-1 or SHP-2 protein levels are shown in the graphs. (**D**, **E**) *In vivo* knockdown of SHP suppressed MAG–Fc-induced dephosphorylation of Trk receptors in retinal cells. Optic nerve extracts were prepared from the eyes injected with SHP-1 (**D**), SHP-2 (**E**), or control siRNA, and the phosphorylation level of TrkB was determined by immunoblotting of the precipitated TrkB. (**F**) Retinal cells were prepared from WT and PIR-B$^{-/-}$ mice. The cells were stimulated with or without MAG–Fc. (**C**–**F**) $^{**}P<0.01$, $^{*}P<0.05$.

stimulation, are required for the effects of MAG on neurite growth inhibition and TrkB dephosphorylation. Thus, PIR-B negatively regulates the basal and/or neurotrophin-regulated levels of Trk activity through SHP-1/2 in postnatal CGNs.

Our findings suggest that a balance in the expression of Trk receptors and PIR-B is critical for the potential of axonal growth following injury. Trk receptors activate key survival and axonal growth regulatory proteins, such as phosphatidylinositol 3-kinase, Akt, and mitogen-activated protein kinase